PCCP

Time-Resolved Quantification of Key Species and Mechanistic Insights in Low-Temperature Tetrahydrofuran Oxidation

Journal:	*Physical Chemistry Chemical Physics*
Manuscript ID	CP-ART-12-2023-006227.R1
Article Type:	Paper
Date Submitted by the Author:	23-Feb-2024
Complete List of Authors:	Demireva, Maria; Sandia National Laboratories Sheps, Leonid; Sandia National Laboratories Au, Kendrew; Sandia National Laboratories Hansen, Nils; Sandia National Laboratories

Submitted to Phys. Chem. Chem. Phys.

Time-Resolved Quantification of Key Species and Mechanistic Insights in Low-Temperature Tetrahydrofuran Oxidation

Maria Demireva,* Kendrew Au, Nils Hansen, and Leonid Sheps*

Combustion Research Facility, Sandia National Laboratories, Livermore, California 94551, USA

*Corresponding authors: E-mail: maria.p.demireva@gmail.com, lsheps@sandia.gov

Abstract

We investigate the kinetics and report the time-resolved concentrations of key chemical species in the oxidation of tetrahydrofuran (THF) at 7500 Torr and 450–675 K. Experiments are carried out using high-pressure multiplexed photoionization mass spectrometry (MPIMS) combined with tunable vacuum ultraviolet radiation from the Berkely Lab Advanced Light Source. Intermediates and products are quantified using reference photoionization (PI) cross sections, when available, and constrained by a global carbon balance tracking approach at all experimental temperatures simultaneously for the species without reference cross sections. From carbon balancing, we determine time-resolved concentrations for the ROO• and •OOQOOH radical intermediates, butanedial, and the combined concentration of ketohydroperoxide (KHP) and unsaturated hydroperoxide (UHP) products stemming from the •QOOH + O_2 reaction. Furthermore, we quantify a product that we tentatively assign as fumaraldehyde, which arises from UHP decomposition via H_2O or •OH + H loss. The experimentally derived species concentrations are compared with model predictions using the most recent literature THF oxidation mechanism of Fenard et al. (*Combust. Flame* 2018, **191**, 252-269). Our results indicate that the literature mechanism significantly overestimates THF consumption and the UHP + KHP concentration at our conditions. The model predictions are sensitive to the rate coefficient for the ROO• isomerization to •QOOH, which is the gateway for radical chain propagating and branching pathways. Comparisons with our recent results for cyclopentane (Demireva et al., *Combust. Flame* 2023, **257**, 112506) provide insights into the effect of the ether group on reactivity and highlight the need to determine accurate rate coefficients of ROO• isomerization and subsequent reactions.

1. Introduction

The oxidation of hydrocarbons and oxygenated molecules in the gas phase consists of a complex network of multi-step pathways.[1-3] The competition among these pathways is influenced by temperature, total pressure, and molecular structure (size and functional group). [4] Understanding such effects in detail can lead to improved predictive modeling of, for example, low-temperature combustion, which can help advance combustion technologies.[5-9]

Cyclic ethers are major intermediates in low-T alkane combustion and can react further.[10] They are also considered as potential next generation biofuels that do not compete with food production but can be created from lignocellulosic biomass.[10-12] The ether group weakens the C-H bonds on the adjacent (α) carbon by 3 – 5 kcal/mol, compared with alkane analogs,[4] leading to preferential H abstraction at the α site. The C-O bond dissociation energy in ether α-radicals is ~12 kcal/mol lower than the C-C bond energy in analogous alkyl radicals,[13] resulting in energetically more favorable ring-opening pathways and overall higher reactivity. Understanding the reactions of cyclic ethers can provide insights into their utility as biofuels and help create more accurate combustion mechanisms. A prototypical cyclic ether is tetrahydrofuran (THF), which has a base molecular structure common to potential biofuels such as 2-methyltetrahydrofuaran and 2,5-dimethyltetrahydrofuran,[11, 14] and which can more generally serve as a model to understand the low-temperature oxidation of cyclic ethers.

Oxidation reactions below ~900 K form either relatively unreactive HO_2 or highly reactive •OH, and can be radical chain inhibiting, propagating, or branching.[1, 2] An overview of the first and second O_2 addition reactions in low-T combustion of a hydrocarbon, RH, is provided in Scheme 1. Included in Scheme 1 are representative structures for the dominant species in the low-T

oxidation of THF,[15] where H abstraction is favored at the α-carbon over the β-carbon because of the weakened C-H bond.[4]

H atom abstraction (typically by •OH) produces fuel radical, R•, that can react with O_2 to produce a peroxy radical, ROO•. ROO• can undergo HO_2 elimination to yield an unsaturated hydrocarbon or isomerize via an internal H-shift to a carbon centered •QOOH radical. In alkanes, •QOOH eliminates •OH and forms a cyclic ether in a radical chain propagating pathway. However, in ethers the weak C-O bond is cleaved concurrently with •OH loss, resulting in the case of THF in the production of a bi-carbonyl species, butanedial, instead of a bi-cyclic ether. •QOOH can also react with a second O_2 molecule to produce a •OOQOOH radical. •OOQOOH can eliminate HO_2 to produce an unsaturated hydroperoxide (UHP) or undergo an internal H shift, followed by •OH elimination to either directly form a ketohydroperoxide (KHP) or to form a cyclic hydroperoxide via a metastable HOO•POOH intermediate (not shown in Scheme 1). At temperatures above ~600 K, hydroperoxides readily decompose to •OH + oxy-radical, enabling further reactions. Thus, the competition among various •OH and HO_2 generating pathways is a key factor controlling low-T reactivity of hydrocarbons. [16]

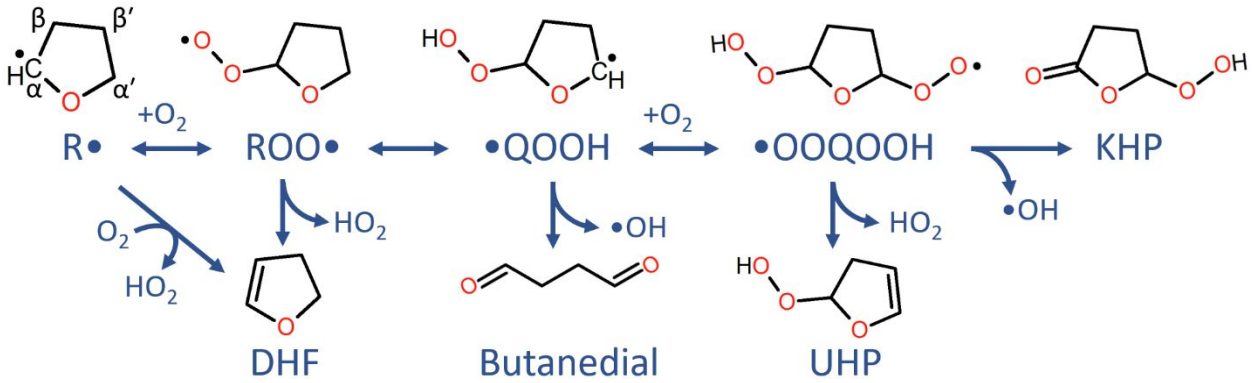

Scheme 1. Simplified schematic of low-temperature hydrocarbon oxidation, along with representative structures for the major species and dominant isomers stemming from the primary α-R• and α,α′-•QOOH radicals in the low-T oxidation of THF.

Several speciation studies have focused on the low-T oxidation of THF and provided mechanistic details.[15, 17-21] Molera et al.[17] employed a static reactor at 493 K, in which they detected 27 oxidation products and found succinic acid to be a major product. Our group recently probed the O_2 and pressure dependent competition between first and second O_2 addition channels in low-T THF oxidation by multiplexed photoionization mass spectrometry (MPIMS).[15] Using deuterium labeling, Antonov et al.[15] found that reactivity in these experiments was dominated by species originating from the α-R• isomer and the most energetically favored α,α′-•QOOH radical (Scheme 1) because of the weaker C-H bonds at the carbons adjacent to the ether group. HO_2 elimination pathways forming dihydrofuran (DHF) and UHP from the ROO• and •OOQOOH peroxy radicals, respectively, were found to be competitive. Furthermore, increased pressure and O_2 concentrations enhanced the formation of •OOQOOH, KHP, and UHP (all from •QOOH + O_2), at the expense of DHF. Jet-stirred reactor (JSR) and rapid compression machine studies were performed by Vanhove et al.[18] for mechanistic insights into low-T THF combustion.

Fenard et al.[22] developed a comprehensive low-T oxidation mechanism incorporating H-atom abstraction rates of THF by •OH from Giri et al.[23] and theory-based rate coefficients for the reactions stemming from R• + O_2. Fenard et al. tested their mechanism against the Vanhove et al. experimental results, and found reasonable agreement.[22] Hansen et al.[20] studied KHP formation in

THF oxidation using a JSR and with the aid of theoretical calculations obtained isomer-resolved information. They estimated that 99% of KHP isomers were formed from the dominant α-R• radical. However, their comparisons with the Fenard et al. mechanism indicated poor agreement with quantified KHP isomers stemming from β-R•. Lockwood and Labbe[24] computed potential energy surfaces for the reactions derived from second O_2 addition to the minor •QOOH isomers in THF oxidation to rationalize the deviations between the experimental results of Hansen et al. and the predictions of the Fenard et al. mechanism. They suggested that the deviations might arise primarily from the uncertainties in H abstraction rates to produce α-R• and β-R•.[24] In recent JSR experiments at 550–620 K, Belhadj et al. [21] detected several highly oxygenated species, some of which were attributed to third O_2 addition (HOO•POOH + O_2) reactions.

In the latest THF low-T JSR study, Koritzke et al.[25] focused on understanding the effect of O_2 concentration on product formation and on providing isomer-resolved detection and quantification of some major species, such as butanedial. Koritzke et al. compared the measured concentrations with model predictions using the Fenard et al. mechanism and a modified version incorporating updated chemistry for furan and 2,3-dihydrofuran from Wu et al.[26] and found discrepancies. In summary, despite significant experimental and theoretical efforts, there appear to be major gaps in our understanding of THF oxidation due to uncertain rate coefficients for key low-T reactions and missing pathways, such as decomposition of UHPs and KHPs.

Development and evaluation of chemical mechanisms relies critically on experimental data, including global measurements, such as ignition delays and flame speeds, and detailed speciation data, for example, from flames and JSRs.[27-29] However, species concentrations from JSR and flame measurements are time-averaged and do not generally capture short-lived intermediates. In contrast, time-resolved speciation experiments, especially those that detect key intermediates, can impose more stringent constraints on models. Except for a few studies involving shock tube measurements,[30] there are not many time-resolved speciation measurements under combustion relevant pressures and temperatures. Recently, we have developed methods to obtain time-resolved concentrations of key intermediates in the low-T oxidation of diethyl ether (DEE),[31] cyclopentane (CPT),[32] and dimethyl ether (DME) [33] using MPIMS. As we have illustrated for CPT,[34] these concentration profiles can serve as valuable targets to constrain mechanism parameters within their expected uncertainties and improve model predictions.

Here, we report new mechanistic information and time-resolved concentrations of key species in the low-T oxidation of THF at 7500 Torr and 450–675 K using MPIMS. Our experiments probe primarily species formed via O_2 addition to the dominant α-R• and α,α′-•QOOH isomers, shown in Scheme 1. We apply a global carbon balance tracking approach, similar to our previous work,[31-33] to determine the time-resolved concentrations for the first time for the key radical intermediates, ROO• and •OOQOOH, and for the major closed-shell intermediate, butanedial. We quantify the combined concentration of UHP and KHP and also quantify a product that we attribute to the decomposition of UHP and tentatively assign as fumaraldehyde. The abundance of fumaraldehyde suggests that HO_2 elimination from •OOQOOH to form UHP is a significant pathway in THF oxidation that needs to be accurately captured in low-temperature THF oxidation mechanisms. Furthermore, the concentration of fumaraldehyde measured here may serve as a valuable constraint in determining the branching into UHP and KHP, which impacts THF reactivity. We compare the present results with our recent work on CPT[32, 34] and with model predictions using the Fenard et al.[22] mechanism. These comparisons highlight the need for accurate determinations of key rate coefficients of reactions stemming from the first and second O_2 addition. The time-resolved concentrations determined in this work offer stringent constraints for the

development, validation, and optimization of low-temperature THF oxidation models.

2. Methods

2.1 Multiplexed photoionization mass spectrometry (MPIMS) experiments

The MPIMS experiments and methodology have been described elsewhere.[35-37] Briefly, we used a high-pressure photolysis reactor coupled with time-of-flight (TOF) mass spectrometry.[35] Flows of THF and Cl_2 or oxalyl chloride ($(COCl)_2$) diluted in He are mixed with pure flows of He and O_2 in a helical static mixer prior to entering the reactor. An excimer laser pulse at 351 nm[38] for Cl_2 or 248 nm[39] for $(COCl)_2$ is used for photolysis to produce Cl atoms that abstract H atoms from THF and initiate reaction. THF does not absorb significantly at 248 or 351 nm. The gas flow velocity is selected to ensure sufficient time to replenish the gas mixture before the next photolysis pulse (5 or 6.667 Hz, allowing for kinetic windows of 250 or 150 ms, respectively).

The reactor is maintained at constant temperature ranging from 450 – 675 K and constant pressure, 7500 Torr. A small central portion of the photolyzed gas mixture exits through a 30 μm diameter pinhole into a vacuum chamber and is intersected by tunable vacuum ultraviolet (VUV) radiation from the Chemical Dynamics Beamline (9.0.2) at the Lawrence Berkeley National Laboratory's Advanced Light Source. Ions produced from the VUV radiation travel through electrostatic focusing optics into an orthogonal acceleration region where they are detected by pulsed reflectron TOF mass spectrometry. The TOF is operated at a 32 kHz repetition rate, acquiring a mass spectrum every 31.25 μs. The photolysis pulse triggers 30 ms after replenishing the gas such that the experimental kinetic window relative to the photolysis pulse at t=0 is -30 to 220 ms if the photolysis laser is operated at 5 Hz. Typical reactant number densities were [THF] = $(1 - 5)\times10^{14}$ cm^{-3}, $[O_2] = (3 - 5)\times10^{18}$ cm^{-3}, $[Cl_2]$ or $[COCl_2] = (1.9 - 2.3)\times10^{15}$ cm^{-3}, and $[Cl](t=0) = (1 - 2)\times10^{13}$ cm^{-3}. Furthermore, we used $[O_2] = 5\times10^{15} - 5\times10^{18}$ cm^{-3} at T = 550 K to explore the effects of O_2 variation on the observed reaction pathways. Experimental conditions are detailed in the Supplementary Information.

By scanning the VUV photon energy, the experiments yield a three-dimensional data set, where ion intensities are obtained as a function of *m*/*z* ratio, time, and photon energy.[36] Such data sets provide information about the chemical composition from accurate mass measurements, species kinetics (e.g., time scales of formation and consumption), and PI spectra (e.g., for identification and quantification from references). As detailed previously,[31, 37] species that have known PI cross sections can be quantified from the measured signals. These signals are first corrected for mass dependent detection bias determined using a calibration mixture of species with known PI cross sections that span the *m*/*z* range of interest. The time-integrated number density of a species, N_x, relative to a reference species, N_{ref}, is then determined using equation (1):

$$N_x = \left(\frac{\sigma_{ref}(E)}{S_{ref}(E)}\right)\left(\frac{S_x(E)}{\sigma_x(E)}\right)N_{ref} \quad (1)$$

S(E) and σ(E) refer to the time-integrated signals and absolute PI cross sections, respectively, of species *x* or the reference compound. Here, THF is used as the reference by correlating the known initial number density to the time-integrated pre-photolysis signal. The time-dependent number density of species *x* is obtained by scaling the measured ion signal such that the time-integrated concentration is equal to N_x.

2.2 Computational methods

Quantum chemical calculations are carried out using the Gaussian16 package.[40] The CBS-QB3[41] composite method is used to calculate adiabatic ionization energies (AIEs) and vertical ionization energies (VIEs) as described before[31] to aid with species assignments from comparison with experimental ionization onsets. Additional calculations are performed that map key regions of the potential energy surfaces (PESs), including intrinsic reaction coordinate scans for transition state (TS) verification, to obtain mechanistic insights, and to aid with species identification.

Chemical kinetics modeling is performed using the open-source package Cantera 2.6.0.[42] The photolysis-initiated experiments are modeled with a zero-dimensional constant pressure and temperature reactor to obtain time-dependent species concentration profiles. The simulations are carried out using the most recent literature mechanism of Fenard et al.[22] for THF oxidation.

3. Results and discussion

3.1 Detected species characterization

The present MPIMS experiments at 7500 Torr reveal many of the same species as those we identified and assigned in our previous study, which focused on the pressure dependent competition among pathways stemming from the first and second O_2 addition at 10 – 2000 Torr.[15] Here, we characterize the PI spectra of the chemical intermediates for which no reference cross sections were previously available and quantify the yields of these intermediates, including two new species that were not discussed in our previous work. The first new species is ROO•. We find that its PI spectrum is dominated by dissociative ionization (DI) into the m/z = 71 fragment, $ROO^+ \rightarrow$ cy-$C_4H_7O^+ + O_2$. However, at this m/z value there is also an interfering signal from a DI fragment of THF ($THF^+ \rightarrow$ cy-$C_4H_7O^+ + H$). Similarly to the approach in our earlier DEE work,[31] we deconvolve the time-dependent signal and PI spectrum of ROO• from the total m/z 71 signal by subtracting the THF DI contribution via its known partial PI cross section into the m/z 71 ion channel.[15] The second new species is detected at m/z = 84 and exhibits slow formation kinetics, and we assign it to a product of UHP decomposition (see below).

Table 1 summarizes the chemical composition, assignments, and m/z values for all major species detected in our MPIMS experiments. Fig. 1 shows the time dependent ion signals, scaled for visual comparison, for a select set of species without reference PI spectra, including m/z 71 (corrected to solely correspond to ROO•), m/z 84 (UHP decomposition product), m/z 103 (DI of •OOQOOH), m/z 58 (DI of butanedial), and m/z 85 (DI of KHP, formed predominantly from α-R• + O_2 + O_2).[15] Note that the UHP, detected at m/z 69 and 102, also has no available reference PI spectrum. However, its ion signals have identical time dependence to those at m/z 85 and are omitted from Fig. 1 for clarity. As shown in Fig. 1, at 550 K and 7500 Torr, ROO• decays rapidly, likely via HO_2 elimination to produce DHF (see Scheme 1) or via isomerization to •QOOH. The carbon-centered •QOOH radical is short-lived and does not accumulate in sufficiently large amount to be detected, reacting via •OH elimination to produce butanedial or with a second O_2 to yield •OOQOOH, and subsequently KHP or UHP.

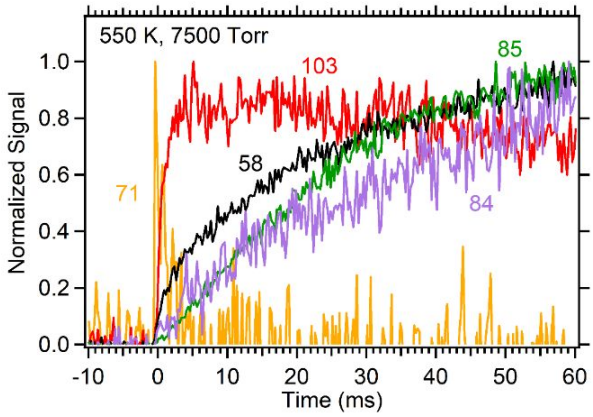

Fig. 1. Representative time signals, measured at 11 eV, of select species produced in Cl-initiated THF oxidation at 550 K and 7500 Torr. The *m/z* 71, 58, 103, and 85 signals correspond to ROO•, butanedial, •OOQOOH, and KHP, respectively. We tentatively assign the *m/z* 84 signal to a UHP decomposition product, fumaraldehyde (see text).

Table 1. Summary of *m/z* peak assignments in the MPIMS experiments.

Species	Ion detected	Co-fragment	*m/z*	Structure[a]
Quantified from reference PI spectra and Antonov et al.[15]				
Ethylene (C_2H_4)	$C_2H_4^+$		28	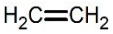
Formaldehyde (CH_2O)	CH_2O^+		30	
Acrolein (C_3H_4O)	$C_3H_4O^+$		56	
DHF (C_4H_6O)	$C_4H_6O^+$		70	
THF-3-one ($C_4H_6O_2$)[b]	$C_4H_6O_2^+$		86	
Assigned from Antonov et al., quantified in this work				
Butanedial ($C_4H_6O_2$)	$C_3H_6O^+$	CO	58	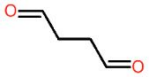
KHP ($C_4H_6O_4$)	$C_4H_5O_2^+$	HO_2	85	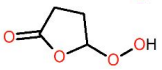
UHP ($C_4H_6O_3$)	$C_4H_6O_3^+$		102	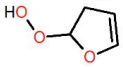
	$C_4H_5O^+$	HO_2	69	
•OOQOOH ($C_4H_7O_5$)	$C_4H_7O_3^+$	O_2	103	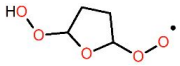
Assigned and quantified in this work.				
ROO• ($C_4H_7O_3$)	$C_4H_7O^+$	O_2	71	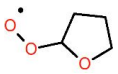
Fumaraldehyde ($C_4H_4O_2$).[c]	$C_4H_4O_2^+$		84	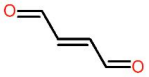

[a] If multiple isomers possible, structure for the expected dominant isomer is shown based on the most energetically favorable pathways of formation.
[b] See Supplementary Information for alternative assignments.
[c] Tentative assignment, see Section 3.2.

3.2 Assignment of *m*/*z* 84 as fumaraldehyde

The *m*/*z* 84 product appears at ~550 K and increases in abundance with increasing temperature. Its rise times are slower than •OOQOOH, but similar to those of UHP and KHP. In addition, the *m*/*z* 84 signal increases with increasing O_2 concentration in the $[O_2] = 5\times10^{15} - 5\times10^{18}$ cm^{-3} range, as shown in the Supplementary Information. These results suggest that the *m*/*z* 84 product arises from a reaction stemming from •QOOH + O_2 via, for example, decomposition of UHP or KHP. In a recent low-T CPT oxidation study[43] that utilized molecular beam VUV photoionization TOF mass spectrometry, an analogous product at *m*/*z* 82 was observed above 700 K and grew in intensity with increasing temperature. The authors attributed this product to H_2O loss from UHP via a four-membered ring TS, formed by the OOH group and the H atom from the same carbon.

The measured PI spectrum (expressed as absolute PI cross section, derived in Section 3.4) for the *m*/*z* 84 product is shown in Fig. 2 and indicates a slow onset around 9.5 eV and a sharper onset at ~10.3 eV. A computed partial PES using the CBS-QB3 composite method that explores H_2O and •OH + H loss channels from UHP is shown in Fig. 3, where the energies are provided relative to the initial reactants, α-R• + O_2 + O_2. Two transition states for H_2O loss are identified. The TS that involves the H atom on the same carbon as the hydroperoxide group is about 5 kcal/mol higher in energy than the TS that involves the H atom on an adjacent carbon. The lower energy H_2O loss pathway yields the co-product cis- or trans-fumaraldehyde, with the trans conformation lower in energy by 4.3 kcal/mol. The computed AIEs for the cis and trans conformations of fumaraldehyde are 9.7 and 10.3 eV, respectively, which are consistent with the slow and sharp onsets observed in the experimental PI spectrum (Fig. 2). The higher energy H_2O loss pathway produces the cyclic species furan-2(3H)-one, which has a calculated AIE of 9.3 eV that is slightly lower than the experimental ionization onset.

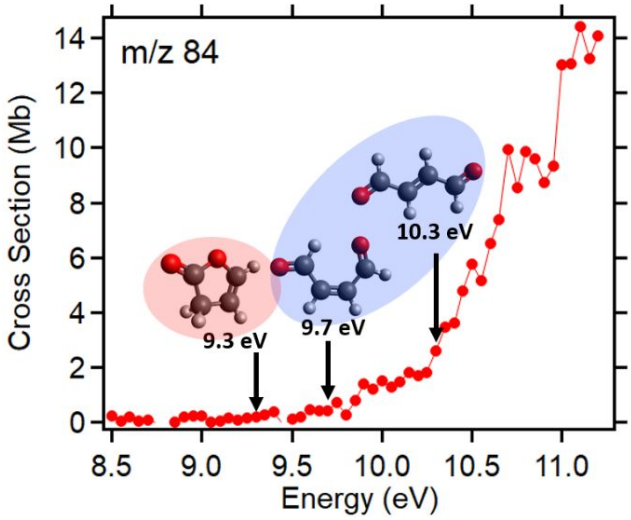

Fig. 2. Absolute PI spectrum from quantification of the detected *m*/*z* 84 species, described in the text, along with computed structures and AIEs of plausible product assignments (using the CBS-QB3 method). The species shaded in red and blue can be formed via the H_2O loss and •OH + H loss pathways from UHP, shown in Fig. 3 with the same color coding.

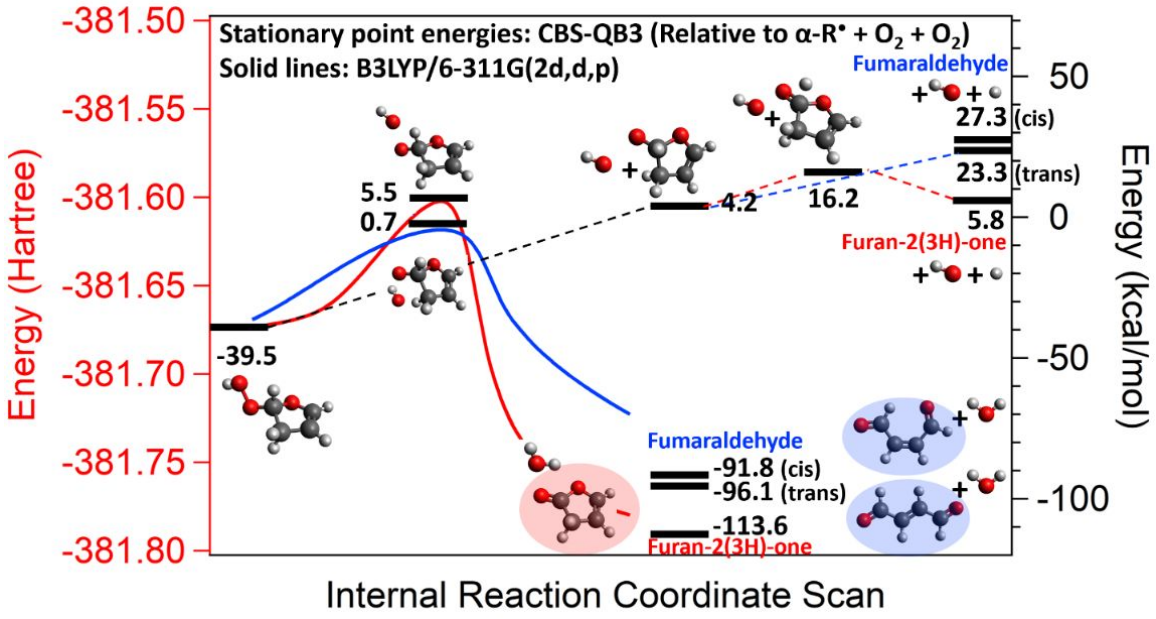

Fig. 3. PES for H_2O and •OH + H loss channels from UHP. Stationary point energies in kcal/mol are calculated with the CBS-QB3 method, relative to α-R• + O_2 + O_2. Internal reaction coordinate scans (red and blue lines) at the B3LYP/6-311G(2d,d,p) level with energies in Hartree are overlaid to show the TSs for the two H_2O loss channels.

The products of the barrierless O-O bond fission, resulting in •OH elimination from UHP, were computed at 4.2 kcal/mol relative to α-R• + O_2 + O_2, ~3.5 kcal/mol above the barrier for the lowest energy H_2O loss pathway. Nonetheless, this fission reaction could be competitive and even dominate the total UHP loss because it is entropically favored, proceeding via a loose TS with no barrier. Subsequent H loss can yield the same *m/z* 84 products as concerted H_2O loss: furan-2(3H)-one via a barrier of 16.2 kcal/mol above α-R• + O_2 + O_2 or fumaraldehyde via barrierless H elimination, lying 23.3 or 27.3 kcal/mol above α-R• + O_2 + O_2 for the trans- or cis-conformer, respectively. This fumaraldehyde pathway should be entropically favored over furan-2(3H)-one.

H_2O_2 elimination from KHP can also yield the products at *m/z* 84, with a partial PES shown in the Supplementary Information. However, lower energy (and entropically favored) pathways such as O-O bond fission leading to •OH loss from KHP (15.8 kcal/mol lower in energy) and isomerization via the Korcek mechanism (9.1 kcal/mol lower) should outcompete the H_2O_2 decomposition channel as discussed further in the Supplementary Information.

To confirm which pathways contribute to the *m/z* 84 products in our experiments, comprehensive theory-based master-equation calculations are needed, which is outside the scope of this paper. Nonetheless, the *m/z* 84 signal appears to arise from fumaraldehyde, produced by •OH + H and/or H_2O elimination from UHP. In section 3.3, we show that it is formed in substantial yields, confirming a general observation that oxidation of cyclic molecules, like THF and CPT, results in a larger amount of UHPs than the oxidation of linear compounds. This trend may be due to stereochemical effects. •QOOH + O_2 can produce two stereoisomers of •OOQOOH, with the peroxy group syn or anti to the OOH group. For THF and CPT, KHP is energetically accessible only from the anti •OOQOOH isomer,[15, 32] whereas HO_2 elimination leading to UHPs is energetically feasible from both •OOQOOH stereoisomers. In contrast, for DEE, a linear molecule, KHPs and UHPs are energetically accessible from both •OOQOOH stereoisomers.[44]

3.3 Quantification of ROO•, •OOQOOH, butanedial, hydroperoxides, and fumaraldehyde

Five species in our experiments are quantified as in our previous THF study,[15] using reference PI cross sections and equation (1): DHF, ethylene, formaldehyde, acrolein, and THF-3-one. Representative fits of the measured PI spectra to reference cross sections are provided in the Supplementary Information. DHF is an HO_2 elimination product of ROO•, whereas ethylene, CH_2O, and acrolein are minor products, most likely of THF-yl ring-opening reactions.[13] We cannot currently explain the formation of THF-3-one, and we discuss possible alternative assignments of the *m/z* 86 species in the Supplementary Information. The temperature dependent concentration profiles for all species are also provided in the Supplementary Information. The contribution of reference-quantified products to the expected carbon-weighted total concentration of products (based on the measured consumption of THF) ranges from ~12% at 450 K to nearly 40% at 675 K, of which DHF contributes ~7% at 450 K and up to 20% at 675 K. These yields are consistent with those from the previous MPIMS study from our group at 10 – 2000 Torr.[15]

The species for which authentic reference samples cannot be obtained, and reference PI cross sections cannot be independently measured, are ROO•, butanedial, •OOQOOH, KHP, UHP and fumaraldehyde. At 450 K and 7500 Torr, only one of these species is present immediately after photolysis: ROO•. The concentration of ROO• can thus be determined by scaling the ROO• signal at early times as shown in Fig. 4 (a) to match the unaccounted product concentration, i.e., the difference between consumed THF and the sum of reference-quantified products. Assuming a temperature-invariant PI cross section, this also allows for the ROO• concentration to be determined at all temperatures of the experiment, as shown in Figure 4 (b).

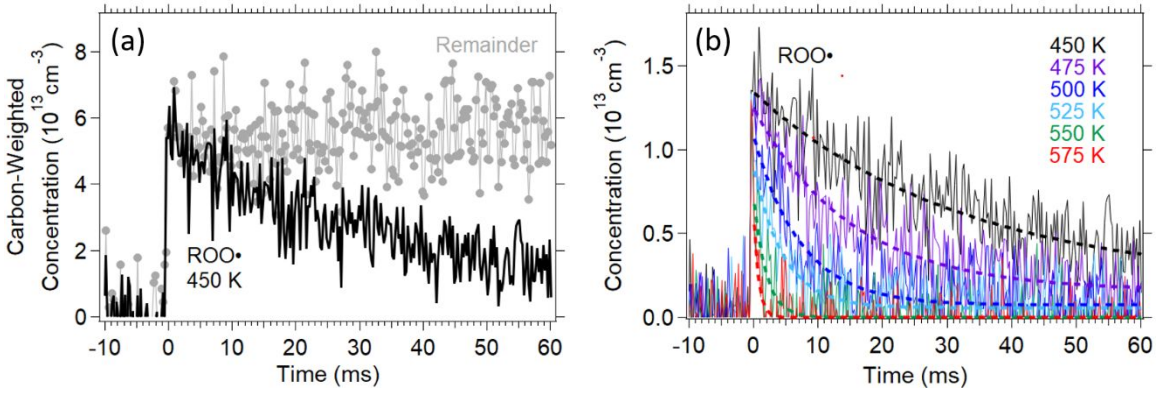

Fig. 4. (a) Time trace of ROO• at 450 K scaled to the carbon-weighted concentration of remaining unquantified products, see text. (b) Time-dependent concentration profiles of ROO• as a function of temperature. The thin lines are experimental data; the thick dashed lines are exponential fits, solely to guide the eye.

The concentrations of the remaining species across all experimental temperatures (450–675 K) are constrained from a global C balance fit to the expected remaining concentration of unquantified products,[31] as shown in Fig. 5. The butanedial, •OOQOOH, total hydroperoxides (KHP + UHP), and fumaraldehyde time signals generally exhibit distinct temperature-dependent kinetics, allowing for a well-constrained fit. However, KHP and UHP exhibit practically identical time dependences and cannot be separately quantified. Instead, their combined concentration is determined, similar to our recent experiments on CPT.[32]

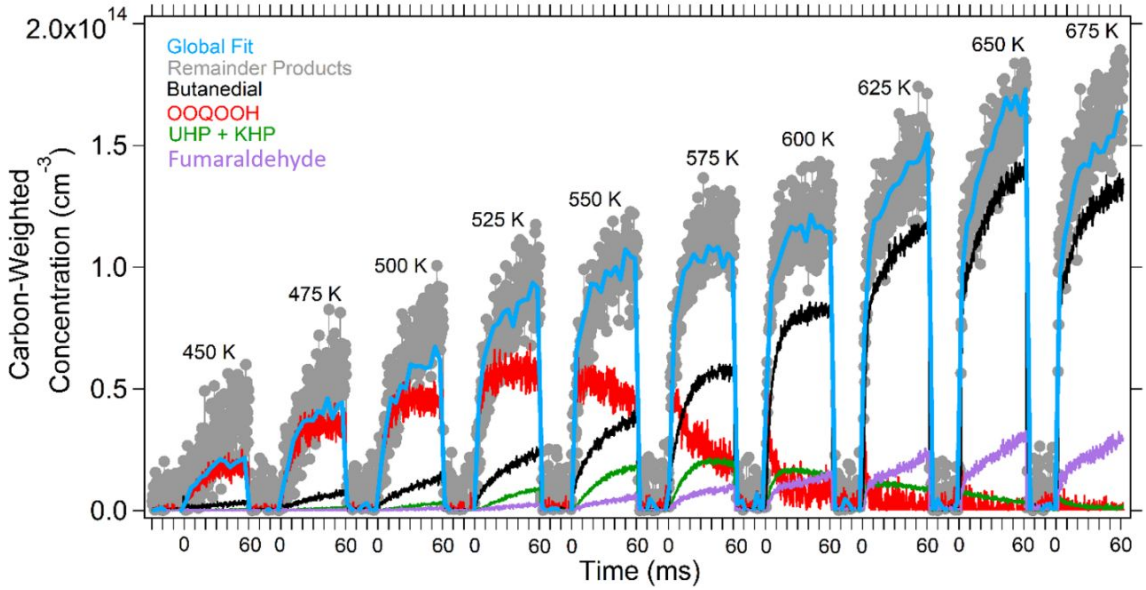

Fig. 5. Global fit of the time dependent signals for butanedial, •OOQOOH, sum of UHP and KHP, and fumaraldehyde, to the expected carbon-weighted concentration of remaining unquantified products across the temperature range of the experiments.

Figures 4 and 5 illustrate that at low temperatures the peroxy intermediates ROO• and •OOQOOH are the major species present on our experimental timescale. At temperatures of 575 K and above, butanedial has the largest concentration, which increases with increasing temperature. In contrast, the combined concentration of KHP and UHP is fairly low and the depletion of these hydroperoxides with increasing temperature coincides with the increasing concentration of fumaraldehyde. As mentioned above, THF-3-one is not easily explained by our reaction mechanism, because its main source should be the β-R• radical, a minor channel in Cl-initiated oxidation. To assess possible systematic errors in our analysis due to mis-assignment of the *m/z* 86 signal to THF-3-one, we replaced its contribution to the overall products with hypothetical other species, whose PI cross section was two times larger or smaller than that of THF-3-one. This modification resulted in a change of ~1% for the quantified concentration of butanedial, ~2 - 6% for •OOQOOH, 5 - 10% for KHP + UHP, and up to 70% for fumaraldehyde. The large uncertainty for fumaraldehyde is due to a strong correlation with the THF-3-one concentration in the C balance fit.

3.4 Photoionization cross sections of ROO•, butanedial, •OOQOOH, and fumaraldehyde

By rearranging equation (1), PI cross sections at the conditions of our experiments can be determined from the quantified concentrations of ROO•, butanedial, and •OOQOOH. The PI cross sections at 11 eV for the DI fragments of ROO• (*m/z* 71), butanedial (*m/z* 58), and •OOQOOH (*m/z* 103) are 7.4±2.6, 16.5±5.8, and 3.0±1.1 Mb, respectively. Fig. 6 shows the measured PI spectra for these species, scaled to match the PI cross sections at 11 eV.

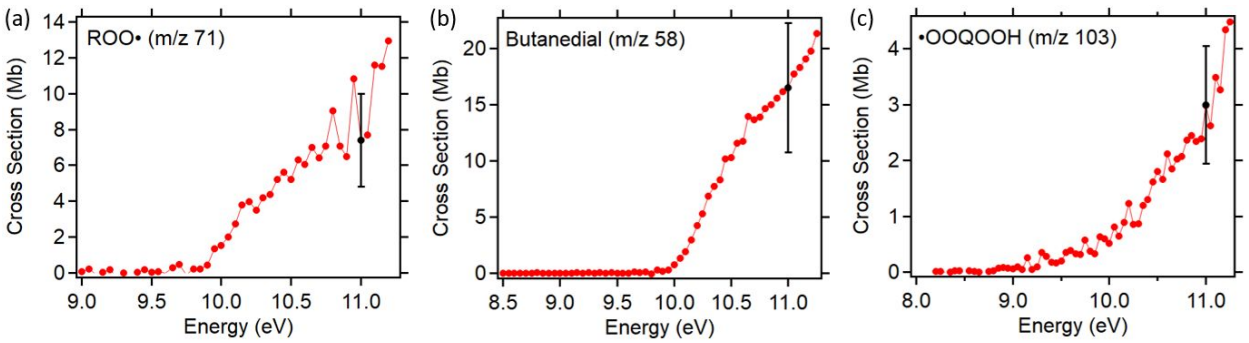

Fig. 6. PI cross sections for the major DI fragments of (a) ROO• (*m/z* 71), (b) butanedial (*m/z* 58), and (c) •OOQOOH (*m/z* 103). Estimated uncertainties discussed in the text are indicated by the error bars at 11 eV.

The *m/z* 71 and 103 ion fragments result from neutral O_2 loss from the peroxy radicals ROO• and •OOQOOH, respectively, which do not form stable parent cations. They are the dominant ion fragments of their respective species we observe up to ionization energy of 11.2 eV, which is significantly higher than the onsets of their ion signals. The absence of strong competing fragmentation channels suggests that their PI cross sections into the *m/z* 71 and 103 ion channels should not depend on temperature. The PI cross section for the DI fragment of ROO• is similar in magnitude and onset to that obtained previously for DEE.[31]

The PI spectrum of the *m/z* 58 ion fragment of butanedial in Fig. 6b is consistent with our previous observation of the photoion yields of this species.[15] The parent ion peak of butanedial is very small (less than 1% of the total photoions), but it has a competing DI pathway into the *m/z* 43 channel, with onset ~ 0.3 eV above the dominant *m/z* 58 channel. Because of this, the partial cross sections determined in this work may depend slightly on temperature, although the total PI cross section should not. The present *m/z* 58 cross section determination places our earlier butanedial photoion yields on the absolute scale, and we provide them in the Supplementary Information. The PI cross section for the *m/z* 84 product, fumaraldehyde, is also determined and is shown in Fig. 2, where the cross section at 11 eV is 13 Mb.

The possible C balance fit errors, associated with mis-assignment of the *m/z* 86 signal to THF-3-one, propagate through Eq. (1) into our PI cross section determinations and contribute errors of <1% for ROO•, up to ~1% for butanedial, and up to 10% for •OOQOOH. Overall, we estimate the uncertainties in the PI cross sections for ROO•, butanedial, and •OOQOOH to be about 35% based on our previous MPIMS quantification results for DEE that take into account systematic and statistical errors.[31] The uncertainty in the fumaraldehyde PI cross section is ~70%, dominated by the correlation with the uncertainty of the THF-3-one yields.

3.5 Comparison between experiment and the most recent THF mechanism

Our time-resolved concentration profiles present stringent tests of performance for the literature THF oxidation mechanisms. We compare select experimental time traces at temperatures of 450 K and 650 K, that typify the low and high-T behavior we observe, to simulations using the mechanism of Fenard et al.[22] in Fig. 7. We chose this mechanism because it is the culmination of many earlier efforts to develop a detailed THF mechanism, it uses key rate coefficients calculated from quantum chemistry, and it has been validated against chemical speciation data from JSRs as well as ignition delay measurements. Concentration profiles are shown in Fig. 7 for THF consumption, and for the formation of ROO•, butanedial, DHF, •OOQOOH, and UHP + KHP.

ROO• and •OOQOOH profiles are provided only at 450 K, because they are not observed at 650 K. As Fig. 7 shows, the simulations significantly overestimate the THF consumption in our experiments. We have previously observed similar deviations for CPT[34] and DEE,[45] where models strongly overpredicted the consumption of the fuel, compared with our MPIMS measurements. Furthermore, the models significantly overpredict our experimental UHP + KHP concentrations (note that the predictions for these species have been scaled down by a factor of 5 in Fig. 7). The butanedial concentration is also overpredicted, as are the production and consumption rates of •OOQOOH. The models reproduce the ROO• and DHF concentrations reasonably well, at the same time as THF is overconsumed, implying that the pathways leading to DHF are underestimated in the mechanism, and the apparent reasonable fit for ROO• is likely accidental.

The significant overprediction of the UHP + KHP concentrations, compared with the experimentally derived concentrations, contributes to the modeled overconsumption of THF. Formation of KHP and subsequent elimination of •OH is a radical chain branching pathway where two •OH radicals are produced for every fuel molecule consumed. Thus, overestimating the flux into the KHP channel will inflate THF reactivity. At the same time, formation of UHP is accompanied by releasing a relatively unreactive HO_2 radical, but subsequent thermal decomposition of UHP into •OH + oxy-radical can also contribute to THF consumption. Although formation and decomposition pathways of UHPs appear to play an important role in our experiments, these channels are generally not considered in the oxidation mechanisms of cyclic hydrocarbons. It appears that experimental strategies to selectively quantify KHPs, UHPs, and their decomposition products are needed to improve the oxidation mechanisms of THF and similar compounds.

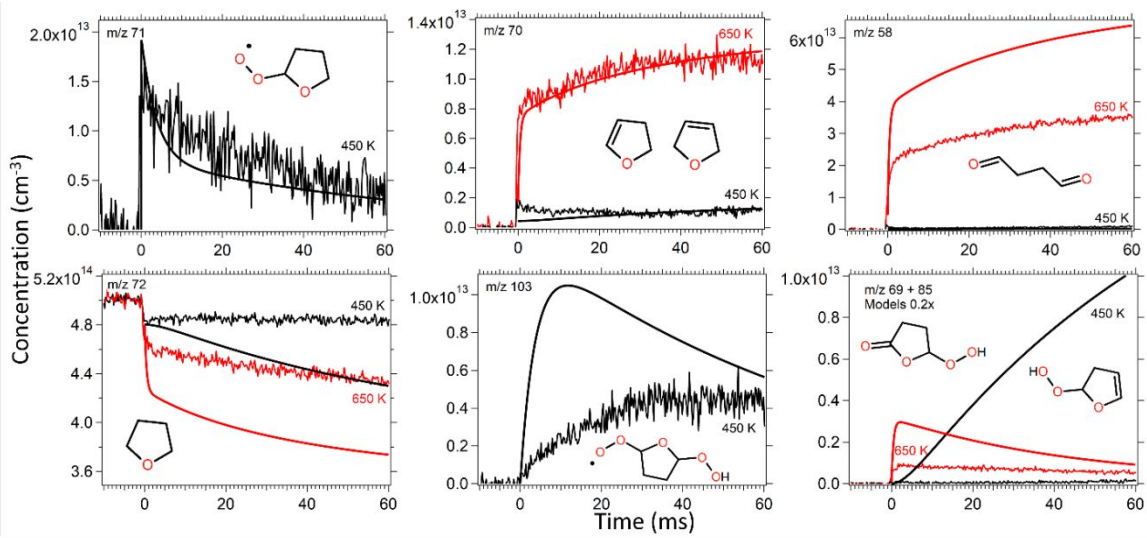

Fig. 7. Comparison of quantified experimental concentration profiles and model predictions using the Fenard et al. mechanism at 450 K and 650 K of key species ROO•, DHF, butanedial, THF, •OOQOOH, and UHP + KHP.

To gain insight into the reactions that might have the largest effect on the modeled concentration profiles, a local sensitivity analysis was carried out for the experiments at 450 and 650 K using the Fenard et al. mechanism, with results summarized in the Supplementary Information. In general, most reactions that have large sensitivity coefficients correspond to those stemming from the first and second O_2 addition. In addition, H abstraction from THF by •OH to

produce α-R• or β-R• also have relatively large sensitivity coefficients. In our recent work on constraining mechanism parameters through genetic algorithm optimization, we found that the modeled species concentrations in MPIMS experiments of CPT oxidation[34] and the mole fractions in JSR experiments on cyclohexane oxidation[46] were sensitive to two key reactions, R1 and R2.

$$\text{ROO•} \leftrightarrow \text{•QOOH} \quad \text{(R1)}$$
$$\text{ROO•} \rightarrow \text{HO}_2 + \text{co-product} \quad \text{(R2)}$$

For the present study, the HO_2 co-product in R2 is DHF, as shown in Scheme 1. For THF, the sensitivity analysis finds R1 to have a large sensitivity coefficient but not R2. Rather, the well skipping reaction, R3, that forms the same products as R2 is found to be sensitive:

$$\text{R•} + \text{O}_2 \rightarrow \text{HO}_2 + \text{DHF} \quad \text{(R3)}$$

The initial steps in THF oxidation involve a dynamic equilibrium between R• + O_2 and the ROO• radicals. Reaction R1 controls the flux from ROO• into radical chain propagating and branching pathways and therefore directly competes with R2 and R3, which are radical chain inhibiting at low temperatures. Although comprehensive mechanism optimization is outside the scope of the current paper, we qualitatively explored the effect of changing the R1 rate coefficient on the modeled fits. Figure 8 demonstrates that reducing k_1 by a factor of 10 largely eliminates both the prompt and long-time overconsumption of THF in our experiments. Note that the uncertainty in k_1 is not known, and the simulations in Fig. 8 are intended not as a fit of k_1, but rather as a visual demonstration of the effect of a large reduction in the isomerization flux on the model. In fact, the KHP and UHP concentrations are still quite overestimated and the concentration profiles for ROO•, DHF, butanedial, and •OOQOOH are not quantitatively reproduced, indicating that further refinement of R1 and the downstream reactions are needed. Yet, the significant improvement in the fits by simply scaling the rate coefficient for the isomerization reaction highlights the large influence this reaction has on THF reactivity.

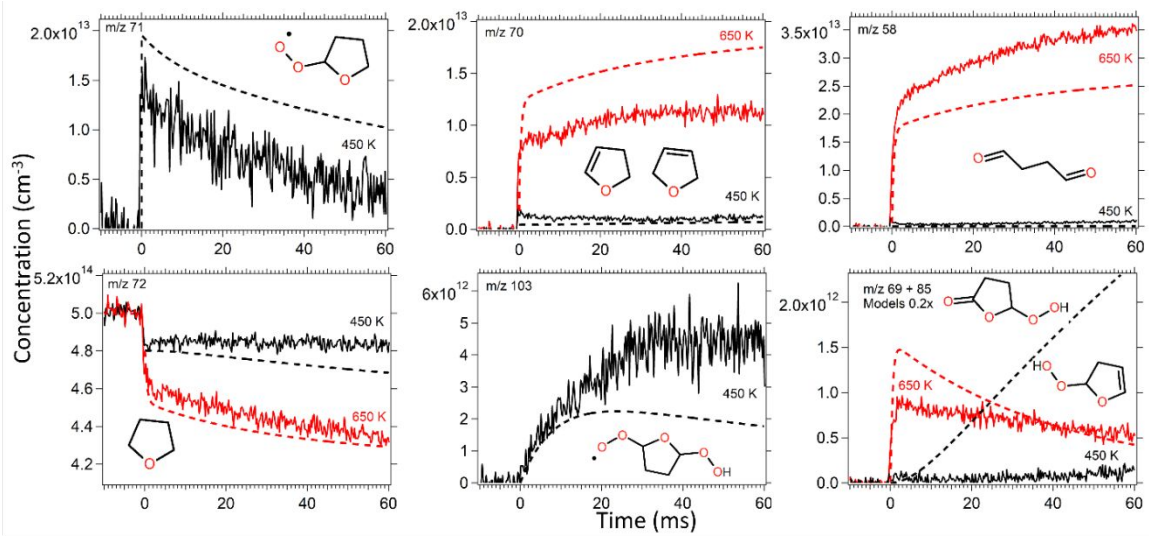

Fig. 8. Comparison of the same quantified experimental concentration profiles from Fig. 7 with new models, where the R1 rate coefficient has been scaled by 0.1 in the Fenard et al. mechanism.

3.6 Competition between ROO• isomerization and HO_2 elimination

Under similar experimental MPIMS conditions at 7500 Torr, THF is significantly more reactive than CPT as shown in Fig. 9 (a). The photolytic Cl atoms rapidly consume ~0.2×10^{14} THF molecules·cm^{-3} at t = 0 ms, followed by secondary THF consumption over t = 0 – 60 ms attributable to radical recycling. The secondary consumption increases dramatically with increasing temperature, which contrasts with the lack of secondary CPT consumption over the same temperature range. Our results are in line with the current consensus that ethers are more reactive than their alkane analogs,[4] and the present time-resolved speciation data shed light on some of the mechanistic reasons for this difference.

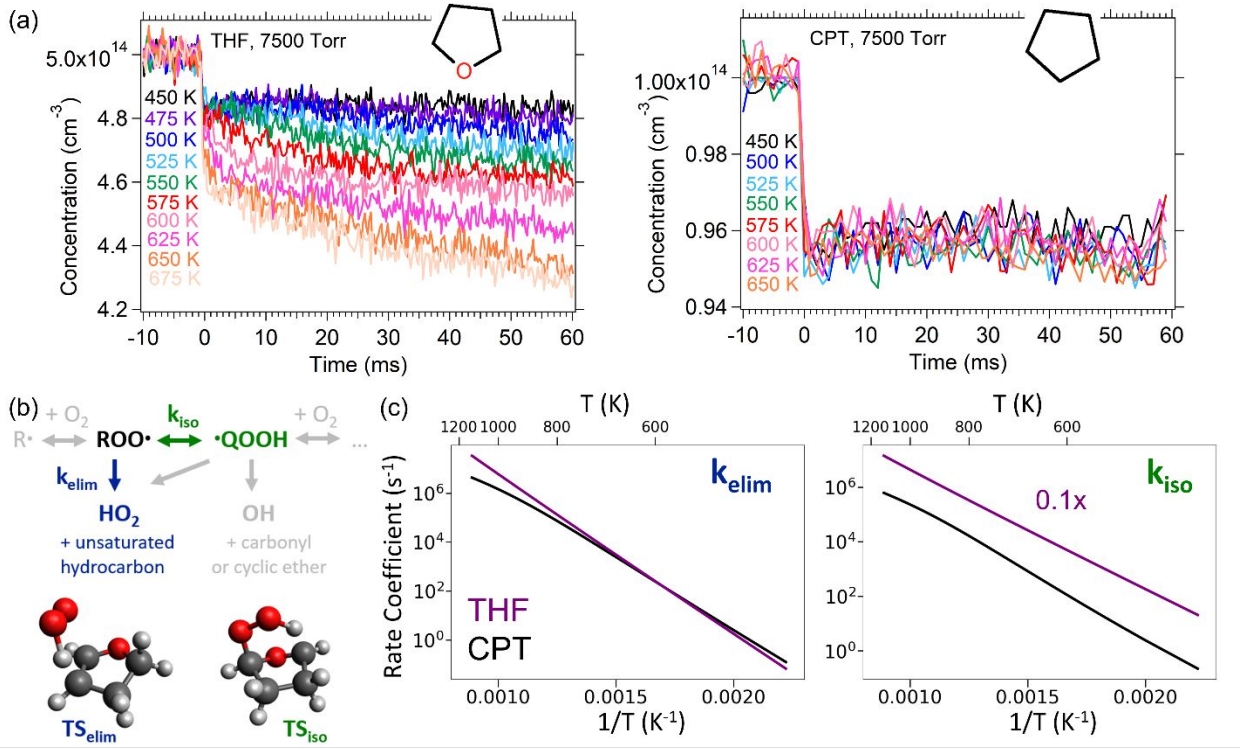

Fig. 9. (a) THF consumption (from this study) and CPT consumption (from ref. 32) as a function of temperature at 7500 Torr under similar MPIMS experimental conditions. (b) Schematic of the ROO• isomerization and HO_2 elimination channels and the corresponding transition state structures for THF, computed with the CBS-QB3 method. (c) Temperature dependent rate coefficients for the HO_2 elimination (k_{elim}) and isomerization (k_{iso}) pathways for THF obtained from the Fenard et al. mechanism and for CPT at 10 bar obtained from our recent work. [34] Note that the isomerization rate coefficients in the Fenard et al. mechanism have been scaled by 0.1.

In our previous work on CPT,[34] the reactivity under our experimental conditions was primarily influenced by the rate coefficients of R1 (isomerization) and R2 (HO_2 elimination), which are schematically shown in Fig. 9 (b). CPT reactivity was dominated by HO_2 elimination from ROO• to form cyclopentene, which is a radical chain inhibiting pathway. In contrast, the dominant product for THF with increasing temperature is butanedial (Fig. 5) produced via •OH elimination from •QOOH – a radical chain propagating pathway. The increased THF reactivity can thus be attributed, in large part, to a larger branching fraction for the ROO• ↔ •QOOH

isomerization relative to HO_2 elimination, compared with the analogous CPT reactions. This is likely due to a larger isomerization rate coefficient because of a lower C-H bond energy on the α-carbon, which lowers the energy barrier for the internal H shift. The isomerization TS structure for THF computed with the CBS-QB3 method is shown in Fig. 9 (b). In contrast, the energy of the HO_2 elimination barrier is likely similar for CPT and THF, because this transition state (Fig. 9 (b)) should not be affected significantly by the ether group.

Temperature dependent CPT rate coefficients for R1 and R2 at 10 bar determined from our previous work[34] are shown in Fig. 9 (c) and are compared with those for THF from the Fenard et al. mechanism, which were reported without pressure dependence. Note that the temperature dependent rate coefficients of THF isomerization in Fig. 9 (c) have been scaled down by a factor of 10 because they reproduced better our experimental results as discussed above. Yet, even the scaled-down k_1 values for THF are much higher than for CPT, whereas the k_2 values for both compounds are similar, which is consistent with our experimentally observed reactivity trend for THF vs. CPT.

Because the isomerization reaction is more favored for THF than for CPT, relative to the HO_2 elimination channel, the reactivity of THF is significantly more complex and is influenced more strongly by radical chain propagating and branching pathways under our conditions. Thus, predicting the THF oxidation chemistry not only requires accurate determinations of the rate coefficients for R1 and R2, but also for the reactions downstream from ROO• isomerization, e.g., •QOOH → butanedial + •OH and the reactions stemming from the second O_2 addition. For example, the •OOQOOH → UHP + HO_2 → oxy-radical + •OH + HO_2 channel overall yields fewer reactive radicals than the competing •OOQOOH → KHP + •OH → oxy-radical + 2 •OH sequence. Thus, the branching between UHP and KHP formation and the fate of their oxy-radical decomposition products is critical to accurately capture the THF low-T chemistry. A combined theory, modeling, and experimental effort might provide the yield of UHPs from model comparisons with the experimental concentrations of the UHP decomposition product fumaraldehyde measured here. Additionally, quantum-chemical calculations of the UHP and KHP decomposition PESs and experiments aimed at quantifying other channel-specific products are clearly needed to constrain the overall THF oxidation mechanism. Ideally, these additional data will include time-resolved quantified concentration profiles, similar to those measured in this work, providing maximal experimental constraints on the THF mechanism development.

4. Conclusions

We report the time-resolved quantification of major species and dominant isomers in THF oxidation at 7500 Torr and 450–675 K using multiplexed photoionization mass spectrometry, coupled with tunable ionizing radiation from the Berkley Lab Advanced Light Source. H atom abstraction of THF by photolytically generated Cl atoms occurred predominantly at the carbon adjacent to the ether group due to a weaker C-H bond energy and produced mainly the α-R• isomer. Reactivity was dominated by first and second O_2 addition reactions of α-R• yielding key peroxy radicals (ROO•, •OOQOOH), hydroperoxides (UHP and KHP), and stable species such as butanedial and dihydrofuran (DHF). We also observed a product with slow formation timescales and assigned it to fumaraldehyde, arising from the decomposition of UHP. Reference photoionization (PI) cross sections were used to quantify minor products detected in the experiments, including formaldehyde, ethylene, acrolein, and DHF. Major species, that lacked reference PI spectra, like ROO• and •OOQOOH, butanedial, total hydroperoxides, and

fumaraldehyde were quantified utilizing their distinct kinetics and fitting against the overall THF consumption in a global carbon balance tracking scheme. Our analysis yielded the PI cross sections for ROO•, •OOQOOH, butanedial, and fumaraldehyde, which can be applied to quantify these species in other experiments.

The detection and assignment of fumaraldehyde suggested that a significant amount of •OOQOOH undergoes HO_2 elimination to produce UHP, which competes with KHP formation and reduces the extent of radical chain branching. More generally, the HO_2 elimination channel to produce UHP is likely important for other cyclic hydrocarbons and impacts their low temperature oxidation chemistry. For THF, a comprehensive low temperature mechanism needs to include the formation pathways to UHP and its decomposition products to correctly capture reactivity. From comparison with models, the experimental concentration of fumaraldehyde can potentially be used to constrain the branching between UHP and KHP formation in THF oxidation.

Simulations were performed using the most recent literature THF oxidation mechanism to compare models with the experimentally derived concentration profiles. The models generally performed poorly against the experimental results, where THF consumption was significantly overpredicted as was the combined concentration of UHP and KHP. Improved agreement with experiment could be achieved by decreasing the rate coefficient for the ROO• to •QOOH isomerization reaction, which is the gateway reaction into radical chain propagating and branching pathways. Comparisons with our recent experimental results for cyclopentane (CPT) oxidation under similar conditions indicated that THF is much more reactive than CPT, which can likely be attributed to larger branching into the ROO• ↔ •QOOH reaction, relative to the competing HO_2 elimination channel. As a result, THF exhibits more complex reactivity than CPT due to increased flux into radical recycling pathways. The modeled reactivity of both CPT and THF is strongly influenced by the rate coefficient for the isomerization reaction highlighting the need for accurate determination of this and other key rate coefficients. Ultimately, time-resolved concentrations offer more stringent model constraints than time-averaged mole fractions by requiring accurate prediction of both the abundance and the kinetic time scales.

Acknowledgements

This work was funded by the U.S. Department of Energy, Basic Energy Sciences (DOE-BES), the Division of Chemical Sciences, Geosciences and Biosciences, through the Argonne-Sandia Consortium on Pressure Dependent Chemistry. The Advanced Light Source is supported by the Director, DOE-BES, under Contract No. DE-AC02-05CH11231. This article was authored by employees of National Technology & Engineering Solutions of Sandia, LLC under Contract No. DE-NA0003525 with the U.S. DOE. The employees own all rights, title, and interest in and to the article and are solely responsible for its contents. The publisher acknowledges that the U.S. Government retains a non-exclusive, paid-up, irrevocable, world-wide license to publish or reproduce the published form of this article or allow others to do so, for U.S. Government purposes. The DOE will provide public access to these results of federally sponsored research in accordance with the DOE Public Access Plan.

Electronic Supplementary Information

Time-resolved species concentration profiles, summary of experimental conditions, additional results for the *m*/*z* 84 product, PI spectra of quantified products from references, possible other assignments of the *m*/*z* 86 product and the effect on quantification, absolute PI cross section of butanedial, and sensitivity analysis.

References

1. F. Battin-Leclerc, O. Herbinet, P. A. Glaude, R. Fournet, Z. Zhou, L. Deng, H. Guo, M. Xie and F. Qi, *Angew. Chem. Int. Ed. Engl.*, 2010, **49**, 3169-3172.
2. J. Zádor, C. A. Taatjes and R. X. Fernandes, *Prog. Energy Combust. Sci.*, 2011, **37**, 371-421.
3. C. L. Heald and J. H. Kroll, *Sci. Adv.*, 2020, **6**, eaay8967.
4. B. Rotavera and C. A. Taatjes, *Prog. Energy Combust. Sci.*, 2021, **86**, 100925.
5. S. J. Klippenstein, *Proc. Combust. Inst.*, 2017, **36**, 77-111.
6. J. A. Miller, R. Sivaramakrishnan, Y. Tao, C. F. Goldsmith, M. P. Burke, A. W. Jasper, N. Hansen, N. J. Labbe, P. Glarborg and J. Zádor, *Prog. Energy Combust. Sci.*, 2021, **83**, 100886.
7. J. E. Dec, *Proc. Combust. Inst.*, 2009, **32**, 2727-2742.
8. X. Duan, M.-C. Lai, M. Jansons, G. Guo and J. Liu, *Fuel*, 2021, **285**, 119142.
9. M. Krishnamoorthi, R. Malayalamurthi, Z. He and S. Kandasamy, *Renew. Sus. Energy Rev.*, 2019, **116**, 109404(109401)-109404(109453).
10. L.-S. Tran, O. Herbinet, H.-H. Carstensen and F. Battin-Leclerc, *Prog. Energy Combust. Sci.*, 2022, **92**, 101019.
11. F. M. A. Geilen, B. Engendahl, A. Harwardt, W. Marquardt, J. Klankermayer and W. Leitner, *Angew. Chem. Int. Ed.*, 2010, **49**, 5510-5514.
12. W. Yang and A. Sen, *Chem. Sus. Chem.*, 2010, **3**, 597-603.
13. J. M. Simmie, *J. Phys. Chem. A*, 2012, **116**, 4528-4538.
14. K. Ulonska, A. Voll and W. Marquardt, *Energy Fuels*, 2016, **30**, 445-456.
15. I. O. Antonov, J. Zador, B. Rotavera, E. Papajak, D. L. Osborn, C. A. Taatjes and L. Sheps, *J. Phys. Chem. A*, 2016, **120**, 6582-6595.
16. Z. Wang, O. Herbinet, N. Hansen and F. Battin-Leclerc, *Prog. Energy Combust. Sci.*, 2019, **73**, 132-181.
17. M. J. Molera, A. Couto and J. A. Garcia-Dominguez, *Int. J. Chem. Kinet.*, 1988, **20**, 673-685.
18. G. Vanhove, Y. Yu, M. A. Boumehdi, O. Frottier, O. Herbinet, P.-A. Glaude and F. Battin-Leclerc, *Energy Fuels*, 2015, **29**, 6118-6125.
19. P. Dagaut, M. McGuinness, J. M. Simmie and M. Cathonnet, *Combust. Sci. Technol.*, 1998, **135**, 3-29.
20. N. Hansen, K. Moshammer and A. W. Jasper, *J. Phys. Chem. A*, 2019, **123**, 8274-8284.
21. N. Belhadj, R. Benoit, P. Dagaut and M. Lailliau, *Energy Fuels*, 2021, **35**, 7242-7252.
22. Y. Fenard, A. Gil, G. Vanhove, H.-H. Carstensen, K. M. Van Geem, P. R. Westmoreland, O. Herbinet and F. Battin-Leclerc, *Combust. Flame*, 2018, **191**, 252-269.
23. B. R. Giri, F. Khaled, M. Szőri, B. Viskolcz and A. Farooq, *Proc. Combust. Inst.*, 2017, **36**, 143-150.
24. K. S. Lockwood and N. J. Labbe, *Proc. Combust. Inst.*, 2021, **38**, 533-541.
25. A. L. Koritzke, N. S. Dewey, M. G. Christianson, S. Hartness, A. C. Doner, A. R. Webb and B. Rotavera, *Combust. Flame*, 2023, **257**, 112640.
26. Y. Wu, N. Xu, M. Yang, Y. Liu, C. Tang and Z. Huang, *Combust. Flame*, 2020, **213**, 226-236.
27. O. Herbinet and F. Battin-Leclerc, *Int. J. Chem. Kinet.*, 2014, **46**, 619-639.
28. F. N. Egolfopoulos, N. Hansen, Y. Ju, K. Kohse-Höinghaus, C. K. Law and F. Qi, *Prog.*

Energy Combust. Sci., 2014, **43**, 36-67.
29. M. Chaos and F. L. Dryer, *Int. J. Chem. Kinet.*, 2010, **42**, 143-150.
30. R. K. Hanson and D. F. Davidson, *Prog. Energy Combust. Sci.*, 2014, **44**, 103-114.
31. M. Demireva, K. Au and L. Sheps, *Phys. Chem. Chem. Phys.*, 2020, **22**, 24649-24661.
32. L. Sheps, A. L. Dewyer, M. Demireva and J. Zádor, *J. Phys. Chem. A*, 2021, **125**, 4467-4479.
33. D. E. Couch, C. R. Mulvihill, R. Sivaramakrishnan, K. Au, C. A. Taatjes and L. Sheps, *J. Phys. Chem. A*, 2022, **126**, 9497-9509.
34. M. Demireva, J. Oreluk, A. L. Dewyer, J. Zádor and L. Sheps, *Combust. Flame*, 2023, **257**, 112506.
35. L. Sheps, I. Antonov and K. Au, *J. Phys. Chem. A*, 2019, **123**, 10804-10814.
36. D. L. Osborn, P. Zou, H. Johnsen, C. C. Hayden, C. A. Taatjes, V. D. Knyazev, S. W. North, D. S. Peterka, M. Ahmed and S. R. Leone, *Rev. Sci. Instrum.*, 2008, **79**, 104103.
37. J. D. Savee, S. Soorkia, O. Welz, T. M. Selby, C. A. Taatjes and D. L. Osborn, *J. Chem. Phys.*, 2012, **136**, 134307.
38. D. Maric, J. P. Burrows, R. Meller and G. K. Moortgat, *J. Photochem. Photobiol. A: Chem.*, 1993, **70**, 205-214.
39. B. Ghosh, D. K. Papanastasiou and J. B. Burkholder, *J. Chem. Phys.*, 2012, **137**, 164315.
40. M. J. Frisch, G. W. Trucks, H. B. Schlegel, G. E. Scuseria, M. A. Robb, J. R. Cheeseman, G. Scalmani, V. Barone, G. A. Petersson, H. Nakatsuji, X. Li, M. Caricato, A. V. Marenich, J. Bloino, B. G. Janesko, R. Gomperts, B. Mennucci, H. P. Hratchian, J. V. Ortiz, A. F. Izmaylov, J. L. Sonnenberg, Williams, F. Ding, F. Lipparini, F. Egidi, J. Goings, B. Peng, A. Petrone, T. Henderson, D. Ranasinghe, V. G. Zakrzewski, J. Gao, N. Rega, G. Zheng, W. Liang, M. Hada, M. Ehara, K. Toyota, R. Fukuda, J. Hasegawa, M. Ishida, T. Nakajima, Y. Honda, O. Kitao, H. Nakai, T. Vreven, K. Throssell, J. A. Montgomery Jr., J. E. Peralta, F. Ogliaro, M. J. Bearpark, J. J. Heyd, E. N. Brothers, K. N. Kudin, V. N. Staroverov, T. A. Keith, R. Kobayashi, J. Normand, K. Raghavachari, A. P. Rendell, J. C. Burant, S. S. Iyengar, J. Tomasi, M. Cossi, J. M. Millam, M. Klene, C. Adamo, R. Cammi, J. W. Ochterski, R. L. Martin, K. Morokuma, O. Farkas, J. B. Foresman and D. J. Fox, *Gaussian 16 Revision B.01*, Wallingford, CT, 2016.
41. J. A. Montgomery, Jr., M. J. Frisch, J. W. Ochterski and G. A. Petersson, *J. Chem. Phys.*, 2000, **112**, 6532-6542.
42. D. G. Goodwin, R. L. Speth, H. K. Moffat and B. W. Weber, Cantera: An Object-Oriented Software Toolkit for Chemical Kinetics, Thermodynamics, and Transport Processes. Version 2.6.0, 2022.
43. Z. Shi, Y. Jiang, J. Yu, S. Chen, J. Chen, Z. Tang and L. Zheng, *Chem. Eur. J.*, 2022, **28**, e202103546.
44. A. D. Danilack, C. R. Mulvihill, S. J. Klippenstein and C. F. Goldsmith, *J. Phys. Chem. A*, 2021, **125**, 8064-8073.
45. C. R. Mulvihill, A. D. Danilack, C. F. Goldsmith, M. Demireva, L. Sheps, Y. Georgievskii, S. N. Elliott and S. J. Klippenstein, *Energy Fuels*, 2021, **35**, 17890-17908.
46. M. Demireva, L. Sheps and N. Hansen, *Energy Fuels*, 2023, **37**, 14240-14253.